

*Linking in-situ charge accumulation to electronic structure in doped SrTiO<sub>3</sub> reveals design principles for hydrogen evolving photocatalysts*

Article

Accepted Version

Moss, B., Wang, Q., Butler, K. T., Grau-Crespo, R. ORCID: <https://orcid.org/0000-0001-8845-1719>, Selim, S., Regoutz, A., Hisatomi, T., Godin, R., Payne, D. J., Katizas, A. G., Domen, K., Steir, L. and Durrant, J. R. (2021) Linking in-situ charge accumulation to electronic structure in doped SrTiO<sub>3</sub> reveals design principles for hydrogen evolving photocatalysts. *Nature Materials*, 20. pp. 511-517. ISSN 1476-1122 doi: <https://doi.org/10.1038/s41563-020-00868-2> Available at <https://centaur.reading.ac.uk/93917/>

It is advisable to refer to the publisher's version if you intend to cite from the work. See [Guidance on citing](#).

To link to this article DOI: <http://dx.doi.org/10.1038/s41563-020-00868-2>

Publisher: Nature Publishing Group

All outputs in CentAUR are protected by Intellectual Property Rights law, including copyright law. Copyright and IPR is retained by the creators or other copyright holders. Terms and conditions for use of this material are defined in

the [End User Agreement](#).

[www.reading.ac.uk/centaur](http://www.reading.ac.uk/centaur)

## **CentAUR**

Central Archive at the University of Reading

Reading's research outputs online

1 **Linking in-situ charge accumulation to electronic structure in doped**  
2 **SrTiO<sub>3</sub> reveals design principles for hydrogen evolving photocatalysts.**

3 Benjamin Moss<sup>1,2</sup>, Qian Wang<sup>3,4</sup>, Keith T. Butler<sup>5</sup>, Ricardo Grau-Crespo<sup>6</sup> Shababa Selim<sup>1,2</sup>,  
4 Anna Regoutz<sup>7</sup>, Takashi Hisatomi<sup>8</sup>, Robert Godin<sup>1,9</sup>, David J. Payne<sup>10</sup>, Andreas Kafizas<sup>1,11</sup>,  
5 Kazunari Domen<sup>6,12</sup>, Ludmilla Steier<sup>1\*</sup> and James R. Durrant<sup>1,2</sup>

---

<sup>1</sup> Department of Chemistry, Imperial College London, London, W12 0BZ, UK

<sup>2</sup> Centre for Plastic Electronics, Imperial College London, Prince Consort Road, London SW7 2BZ, UK

<sup>3</sup> Department of Chemical System Engineering, School of Engineering, The University of Tokyo, 7-3-1 Hongo, Bunkyo-ku, Tokyo 113-8656, Japan

<sup>4</sup> Department of Chemistry, University of Cambridge, Lensfield Road, Cambridge CB2 1EW, UK

<sup>5</sup> SciML, Scientific Computing Division, Rutherford Appleton Laboratory, Harwell, OX11 0QX, UK

<sup>6</sup> Department of Chemistry, University of Reading, Whiteknights, Reading, RG6 6AD, UK

<sup>7</sup> Department of Chemistry, University College London, 20 Gordon Street, London, WC1H 0AJ, UK

<sup>8</sup> Research Initiative for Supra-Materials, Interdisciplinary Cluster for Cutting Edge Research, Shinshu University, 4-17-1 Wakasato, Nagano-shi, Nagano 380-8553, Japan

<sup>9</sup> Department of Chemistry, University of British Columbia, Kelowna, BC, V1V 1V7, Canada

<sup>10</sup> Department of Materials, Imperial College London, London, SW7 2AZ, UK

<sup>11</sup> Grantham Institute, Imperial College London, London, SW7 4AZ, UK

<sup>12</sup> Office of University Professor, The University of Tokyo, 7-3-1 Hongo, Bunkyo-ku, Tokyo 113-8656, Japan

\* correspondence to: l.steier@imperial.ac.uk

## 6 Abstract

7 Recently, record solar to hydrogen efficiencies have been demonstrated using La,Rh co-  
8 doped SrTiO<sub>3</sub> (La,Rh:SrTiO<sub>3</sub>) incorporated into a low cost and scalable Z-scheme  
9 device, known as a photocatalyst sheet. However, the unique properties that enable  
10 La,Rh:SrTiO<sub>3</sub> to support this impressive performance are not fully understood.  
11 Combining in-situ spectroelectrochemical measurements with density functional theory  
12 and photoelectron spectroscopy produces a depletion model of Rh:SrTiO<sub>3</sub> and  
13 La,Rh:SrTiO<sub>3</sub> photocatalyst sheets. This reveals remarkable properties, such as deep  
14 flatband potentials (+2 V<sub>RHE</sub>) and a Rh oxidation state dependent reorganisation of the  
15 electronic structure, involving the loss of a vacant Rh 4d mid gap state. This  
16 reorganisation enables Rh:SrTiO<sub>3</sub> to be reduced by co-doping without compromising p-  
17 type character. In-situ time resolved spectroscopies show the electronic structure  
18 reorganisation induced by Rh reduction controls electron lifetime in photocatalyst  
19 sheets. In Rh:SrTiO<sub>3</sub>, enhanced lifetimes can only be obtained at negative applied  
20 potentials, where the complete Z-scheme operates inefficiently. La co-doping fixes Rh in  
21 the 3+ state, resulting in long-lived photogenerated electrons even at very positive  
22 potentials (+1 V<sub>RHE</sub>), where both components of the complete device operate effectively.  
23 This understanding of role of co-dopants provides new insight into the design principles  
24 for water splitting devices based on bandgap engineered metal oxides.

25  
26 Wide band gap binary and ternary metal oxides such as TiO<sub>2</sub>,<sup>1</sup> SrTiO<sub>3</sub>,<sup>2</sup> are often considered  
27 benchmark photocatalysts due to their chemical stability, low-cost and high quantum yields  
28 (>70% for unassisted water splitting).<sup>3,4</sup> However, their large optical band gap limits solar  
29 harvesting to the UV and solar-to-hydrogen (STH) conversion efficiency to ~2%.<sup>5</sup> One  
30 potential strategy to introduce visible light absorption is to modify the band structure of wide  
31 band gap oxides. For example, visible light harvesting in TiO<sub>2</sub> has been achieved through  
32 doping with carbon<sup>6</sup>, nitrogen<sup>7</sup> or transition metals.<sup>8,9</sup> Improvements have been chequered,  
33 uncovering significant challenges in translating enhanced visible light harvesting into  
34 improved STH efficiency.<sup>1,10</sup> With notable exceptions,<sup>6,7</sup> marginal gains or even losses in  
35 overall photon conversion efficiency are generally observed in most studies, despite  
36 improved light absorption.<sup>9,11,12</sup> The reasons for these losses are often unclear, but are  
37 broadly attributed to the inadvertent formation of localised dopant states, associated with  
38 short carrier diffusion lengths and low conductivities, and/or charge compensating defect  
39 levels, which may act as recombination centres.<sup>13,14</sup> As such, doping for visible light activity  
40 has often been suggested to be a less promising strategy for producing efficient  
41 photocatalysts in comparison to other methods.<sup>14,15-22</sup>

42 Recently Domen and co-workers have demonstrated a band gap engineered wide band gap  
43 oxide (La,Rh co-doped SrTiO<sub>3</sub>) exhibiting QYs in the visible of 33% and overall STH  
44 efficiencies exceeding 1% using a 'photocatalyst sheet' device architecture.<sup>23-26</sup> This  
45 represents a record for a Z-scheme water splitting device. Sheets are constructed by  
46 embedding a layer of n-type Mo:BiVO<sub>4</sub> and p-type La,Rh:SrTiO<sub>3</sub> semiconducting particles  
47 into a solid conductive mediator such as gold or carbon. Pioneering ex-situ studies of  
48 Rh:SrTiO<sub>3</sub><sup>27-31</sup> powders have indicated that Rh<sup>4+</sup> substitution at Ti<sup>4+</sup> sites introduces filled Rh  
49 states above the SrTiO<sub>3</sub> valence band (VB) as well as a vacant mid gap state.<sup>27</sup> Reduction of  
50 Rh<sup>4+</sup> to Rh<sup>3+</sup> by chemical reduction or co-doping suppresses this state.<sup>27,29</sup> Electron trapping in  
51 Rh:SrTiO<sub>3</sub> has been previously observed in ex-situ transient absorption experiments on  
52 nanosecond timescales and was attributed to trapping in the vacant mid gap state, thus  
53 explaining the low efficiency of Rh<sup>4+</sup> doped systems.<sup>11-14</sup> However, the absence of a  
54 semiconductor electrolyte interface in these studies means that the intrinsic capacity of  
55 Rh:SrTiO<sub>3</sub> and related materials to separate charge remains unexplored. Further, key



operational parameters such as the potential drop when contacted with electrolyte remain unmeasured, limiting understanding of the factors that may facilitate charge separation in this remarkable material.<sup>27,29</sup> Herein, we combine time resolved optical spectroscopies performed in situ on (La),Rh: SrTiO<sub>3</sub> photocatalyst sheets with direct electronic structure measurements supported by density functional theory (DFT) to reveal the remarkable interplay between Fermi level position, Rh 4d structure and band bending/charge separation in Rh: SrTiO<sub>3</sub> materials.

Figures 1a-b show optical absorption spectra and photographs of SrTiO<sub>3</sub>, Rh: SrTiO<sub>3</sub>, hydrogen reduced Rh: SrTiO<sub>3</sub> (H<sub>2</sub>-Rh: SrTiO<sub>3</sub>) and La, Rh: SrTiO<sub>3</sub> powders used to fabricate photocatalyst sheets. XRD showed all powders to be phase pure – consisting of single perovskite phase (Supplementary Fig. S0). Upon doping SrTiO<sub>3</sub> with Rh, a purple powder is obtained showing a 0.4 eV red-shift in the effective optical band gap (Tauc plots in Supplementary Fig. S1) alongside two strongly broadened sub-bandgap absorption features between ~500-800 nm and ~900-1200 nm. After chemically reducing Rh: SrTiO<sub>3</sub> in a hydrogen atmosphere, the powder turns bright yellow and the absorption spectrum shows a further red-shift in the effective band edge and the disappearance of the additional absorption features, consistent with previous observations.<sup>8,27</sup> XPS indicates the reduction of Rh<sup>4+</sup>, predominantly to Rh<sup>3+</sup> (Supplementary Fig. S2.1-S2.3). A similar effect is observed when Rh: SrTiO<sub>3</sub> is co-doped with La. Here, a light-yellow powder is obtained. XPS reveals a Rh:La ratio of 1:1 in our samples and the reduction of Rh<sup>4+</sup> to Rh<sup>3+</sup>. This is in agreement with previous studies which reported that La<sup>3+</sup> substitution at Sr<sup>2+</sup> sites can effectively facilitate the reduction of Rh<sup>4+</sup> to Rh<sup>3+</sup> via an ionic charge compensation mechanism,<sup>23,29,30</sup> and shows that La co-doping has an effect analogous to chemical reduction.

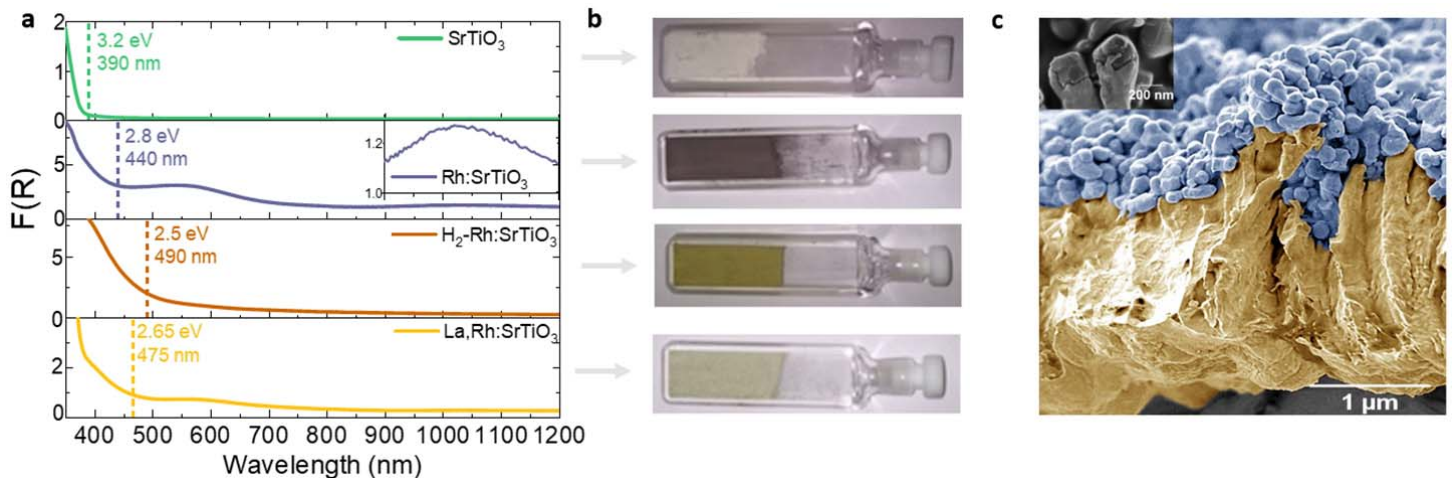


**Figure 1. The colour of doped and undoped SrTiO<sub>3</sub> powders and the morphology of photocatalyst sheets.** (a) Optical absorption spectra, plotted in dimensionless units of the Kubelka-Munk function, F(R), for SrTiO<sub>3</sub>, Rh doped SrTiO<sub>3</sub> (Rh: SrTiO<sub>3</sub>), hydrogen reduced Rh: SrTiO<sub>3</sub> (H<sub>2</sub>-Rh: SrTiO<sub>3</sub>) and La, Rh co-doped SrTiO<sub>3</sub> (La, Rh: SrTiO<sub>3</sub>). Dotted lines show the fitted effective optical band gap extracted from Supplementary Fig. S1. (b) Photographs of the powders to indicate the color of the aforementioned materials. (c) A typical cross-sectional SEM image of the photocatalyst sheets studied herein, showing a monolayer of partially sintered (La), Rh: SrTiO<sub>3</sub> particles (blue) embedded (see inset) in a 2 μm thick gold back contact (yellow). This is colored according to EDX mapping results (Supplementary Fig. S3).

We fabricated photocatalyst sheet half-electrodes from these powders using a modified particle transfer method (see Methods). Cross-sectional scanning electron microscopy (SEM) images (Fig. 1c, EDX mapping in Supplementary Fig. S3) show that these modified photocatalyst sheets consist of a layer of partially sintered oxide particles embedded in a 2 μm thick Au back contact. These photocatalyst sheet half-electrodes permit us to study the properties of Rh: SrTiO<sub>3</sub> and La, Rh: SrTiO<sub>3</sub> under operational conditions, meaning in electrolyte solution, under illumination and in the potential window a z-scheme device is

86 likely to operate during water splitting. As such the results shown in Figure 2 track electrode  
87 processes and transformation in situ and thus differ from ex situ studies published thus far.  
88 Spectroelectrochemical (SEC) measurements of a Rh:SrTiO<sub>3</sub> photocatalyst sheet shown in  
89 Figure 2a track the change in optical absorption at the surface of Rh:SrTiO<sub>3</sub> as the potential is  
90 varied from 1.1 V<sub>RHE</sub> towards -0.2 V<sub>RHE</sub>. The differential absorption spectra at more negative  
91 potentials show a redshift in absorption around the effective band edge (positive  $\Delta F(R)$ ) that  
92 occurs in concert with the loss of absorption from the sub-band gap features (negative  
93  $\Delta F(R)$ ). This trend is reversible when the potential is scanned in the opposite direction  
94 (Supplementary Fig. S4a).  $\Delta F(R)$  of the sub-band gap features exhibits sigmoidal behaviour  
95 with respect to applied potential, typical of a redox couple, with  $E_{1/2}$  located at 0.52 V<sub>RHE</sub>  
96 (Supplementary Fig. S4b and Fig. 2f discussed further below). A similar differential  
97 absorption spectrum can be obtained by subtracting the absorption spectrum of (Rh<sup>4+</sup>)  
98 Rh:SrTiO<sub>3</sub> from (Rh<sup>3+</sup>) H<sub>2</sub>-Rh:SrTiO<sub>3</sub> (Fig. 2b). We therefore attribute the optical changes  
99 observed in Rh:SrTiO<sub>3</sub> photocatalyst sheets under applied potential to the reversible  
100 reduction of Rh<sup>4+</sup> to Rh<sup>3+</sup> within the space charge layer. This is corroborated by cyclic  
101 voltammograms showing a reversible redox wave within the same potential window  
102 (Supplementary Fig. S4c). In contrast, the optical absorption of La,Rh:SrTiO<sub>3</sub> sheets shows  
103 negligible absorption changes over this potential range (Supplementary Fig. S4d), consistent  
104 with an ionic charge compensation mechanism, which fixes Rh predominantly in the 3+  
105 oxidation state independent of applied bias.

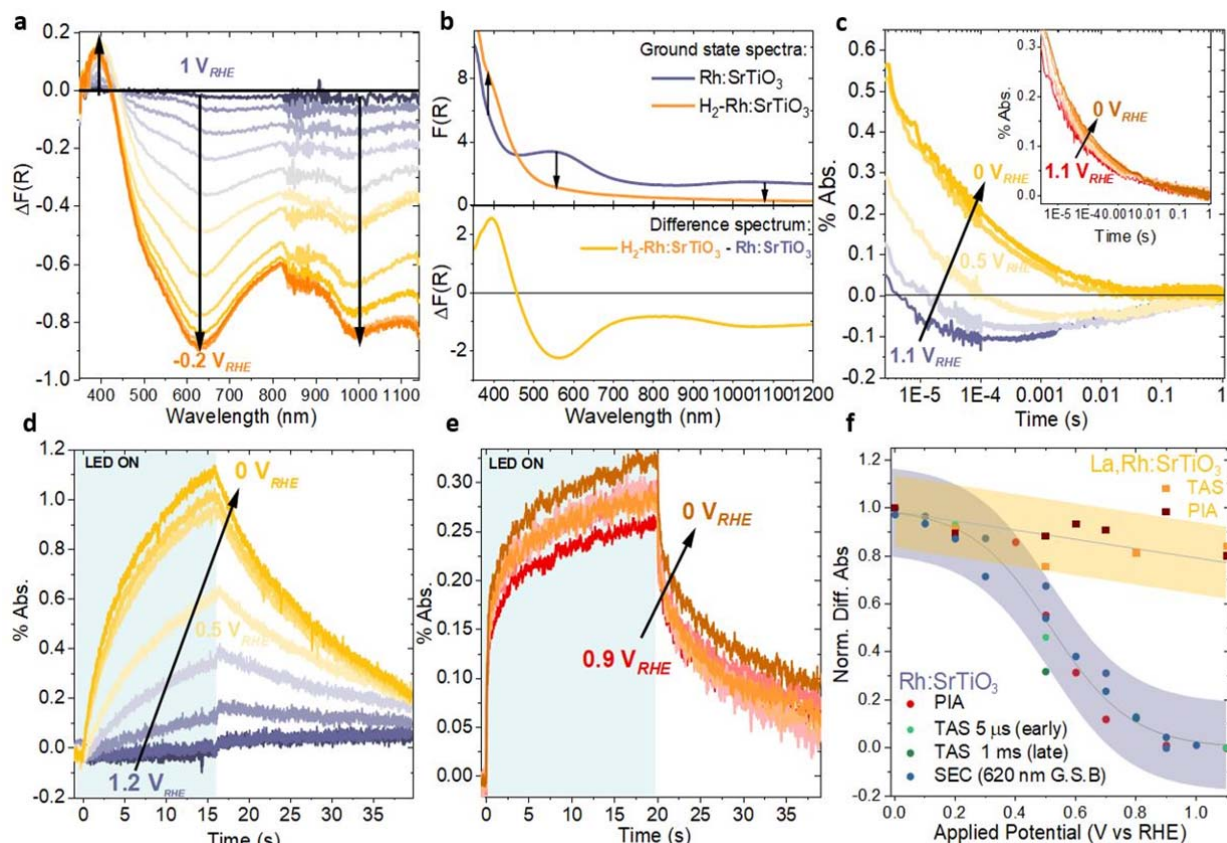


**Figure 2. Connecting the Rh oxidation state to charge carrier dynamics of (La,Rh):SrTiO<sub>3</sub> photocatalyst sheets.** (a) Spectroelectrochemical (SEC) difference spectra of Rh:SrTiO<sub>3</sub> photocatalyst sheets, showing the change in optical absorption upon applying negative potentials in comparison to a reference spectrum taken at 1.1 V<sub>RHE</sub> [ $\Delta F(R) = F(R(V_{\text{applied}})) - F(R(1.1 V_{\text{RHE}}))$ ]. (b) The absorption spectra of Rh:SrTiO<sub>3</sub> and H<sub>2</sub>-Rh:SrTiO<sub>3</sub> (top) can be subtracted to produce a difference spectrum [ $\Delta F(R) = F(R(\text{H}_2\text{-Rh:SrTiO}_3)) - F(R(\text{Rh:SrTiO}_3))$ ] (bottom) similar to that seen in (a). (c) Transient absorption kinetics of electrons in Rh:SrTiO<sub>3</sub> and La,Rh:SrTiO<sub>3</sub> (inset) photocatalyst sheets measured over a range of applied potentials (1.1, 0.8, 0.5, 0.3 and 0 V<sub>RHE</sub>). Samples were excited with a 355 nm laser pulse (7 ns, 400  $\mu\text{J}/\text{cm}^2$ ) with a 1250 nm probe light used to monitor electrons. (d) Photoinduced absorption (PIA) kinetics in Rh:SrTiO<sub>3</sub> and (e) La,Rh:SrTiO<sub>3</sub> photocatalyst sheets at various applied potentials, tracking conduction band electrons monitored at 1250 nm. The sample was irradiated with 365 nm LED light for several seconds (8 mW cm<sup>-2</sup>, shaded region) before the LED was switched off again. (f) Overlay of normalised differential absorption as a function of potential extracted from: i) the 620 nm bleaching signal in SEC, normalised against the bleaching minimum at 620 nm and 0 V<sub>RHE</sub> (Fig. 2a) ii) TA signals measured at 5  $\mu\text{s}$  and 1 ms normalised against the 0 V<sub>RHE</sub> signal at these times (Fig. 2c) and iii) the maximum PIA amplitude, normalised using the PIA maximum at 0 V<sub>RHE</sub> (Fig. 2d,e) for Rh:SrTiO<sub>3</sub> and La,Rh:SrTiO<sub>3</sub> photocatalyst sheets. All data points for Rh:SrTiO<sub>3</sub> sheets were then fitted to a sigmoidal (logistic decay type) function, yielding a midpoint at 0.52 V<sub>RHE</sub>. A linear function was used to fit datapoints for La,Rh:SrTiO<sub>3</sub> sheets. Electrolyte in all measurements: 0.1 M Na<sub>2</sub>SO<sub>4</sub> solution (pH 7).

106 Figure 2c shows potential dependent transient absorption (TA) of (La,Rh):SrTiO<sub>3</sub>  
 107 photocatalyst sheet half-electrodes. We excited samples with a UV laser flash and monitored  
 108 the kinetics at 1250 nm, spanning the  $\mu\text{s}$ -s timescales relevant to water splitting reactions<sup>32</sup>.  
 109 TA studies of SrTiO<sub>3</sub> and La,Rh:SrTiO<sub>3</sub> using electron and hole scavengers (Supplementary  
 110 Fig. S5.1-5.2) indicate that 1250 nm probes the absorption of photogenerated electrons  
 111 relatively close in energy to the conduction band (hereafter ‘CB electrons’, though we note  
 112 that in oxide materials these CB electrons are not necessarily of the same nature as early  
 113 timescale (i.e. ps-ns) free electrons in the CB). In La,Rh:SrTiO<sub>3</sub> sheets (inset Fig. 2c), a  
 114 positive 1250 nm transient absorption is observed, showing power law decay kinetics  
 115 invariant over the range of potentials studied (TA analysis in Supplementary Fig. 5.3a). Only  
 116 a modest initial amplitude dependence on applied potential (<10%) is found. In the case of  
 117 Rh:SrTiO<sub>3</sub> photocatalyst sheets, the TA kinetics show two distinct decay regimes governed  
 118 by applied potential. At positive potentials (e.g. 1.1 V<sub>RHE</sub>) a transient bleach (loss of

119 absorption) is observed on the  $\mu\text{s}$ -ms timescale. SEC of Rh:SrTiO<sub>3</sub> sheets (Fig. 2a) indicates  
120 that a loss of sub-band gap absorption is associated with the removal of Rh<sup>4+</sup> states from the  
121 system. Consequently, we attribute the 1250 nm bleach observed in Rh:SrTiO<sub>3</sub> sheets at  
122 positive applied potentials to a loss of Rh<sup>4+</sup> states after excitation, presumably related to  
123 electron trapping by Rh<sup>4+</sup> states. This is in agreement with *ex-situ* observations made by  
124 Murthy *et al*<sup>33</sup> and is also concordant with a linear dependence of the amplitude of this  
125 feature on laser intensity (Supplementary Fig. 5.3b,c). In contrast, at potentials close to 0  
126  $V_{RHE}$ , positive transients are observed with power law decay kinetics *identical* to  
127 La,Rh:SrTiO<sub>3</sub> (Supplementary Fig. S5.3d). By extension, we therefore also assign absorption  
128 at 1250 nm in Rh:SrTiO<sub>3</sub> sheets at negative applied potentials to CB electrons. A change in  
129 the fate of photogenerated electrons in Rh:SrTiO<sub>3</sub> photocatalyst sheets is further supported by  
130 the TA spectrum of Rh:SrTiO<sub>3</sub> (Supplementary Fig. S5.4a), which is similar to La,Rh:SrTiO<sub>3</sub>  
131 at negative potentials but dissimilar at positive potentials (Supplementary Fig. S5.4b).  
132 To evaluate photocatalyst sheets under operational conditions and study the accumulation of  
133 charges at the oxide surface available for catalysis, we monitored electron dynamics (1250  
134 nm probe) during and after long pulse illumination (15-20s) with a 365 nm LED (Fig. 2d-e  
135 and Methods). The resulting photoinduced absorption (PIA) spectra of Rh:SrTiO<sub>3</sub> and  
136 La,Rh:SrTiO<sub>3</sub> sheets (Supplementary Fig. S5.5a-c) exhibit a similar shape and potential  
137 dependence to the respective TA spectra (Supplementary Fig. 5.4a,b), indicating that the  
138 same species are monitored at 1250 nm in both experiments. We observe that electron  
139 accumulation during irradiation is strongly potential-dependent in Rh:SrTiO<sub>3</sub> photocatalyst  
140 sheets (Fig. 2d), but broadly potential-independent in La,Rh:SrTiO<sub>3</sub> sheets (Fig. 2e). At  
141 positive potentials (e.g. 1.1  $V_{RHE}$ ) Rh:SrTiO<sub>3</sub> shows a small ground state bleach. This signal  
142 transforms into a growing positive absorption as the applied potential approaches 0  $V_{RHE}$ .  
143 After the LED is turned off, the small bleach signal at positive applied potentials recovers on  
144 a similar timescale ( $\sim$ 100 ms) to that seen in TAS (Fig. 2c). In contrast, at negative potentials,  
145 absorption signals persist for tens of seconds after the LED is turned off.  
146 Figure 2f summarises the potential dependence of our in-situ studies; plotting signal  
147 amplitudes of SEC (Fig. 2a), TA (Fig 2c) and PIA (Fig. 2d,e) against electrode potential for  
148 Rh:SrTiO<sub>3</sub> and La,Rh:SrTiO<sub>3</sub> photocatalyst sheets. In Rh:SrTiO<sub>3</sub> photocatalyst sheets,  
149 normalised TA signals, as well as the maximum PIA amplitude of accumulated electrons  
150 track the redox wave behaviour of our SEC measurements (Supplementary Fig. S4b). This  
151 overlay clearly shows that the photogeneration of long-lived conduction band electrons is  
152 strongly linked to Rh<sup>4+</sup> reduction in Rh:SrTiO<sub>3</sub> sheets. In summary, this data indicates that  
153 under operational conditions, Rh:SrTiO<sub>3</sub> photocatalyst sheets only generate long-lived  
154 electrons for biases  $\ll$  0.52  $V_{RHE}$  (i.e.  $E^{Rh^{4+}/Rh^{3+}}$ ), whilst La,Rh:SrTiO<sub>3</sub> sheets produce  
155 long-lived electrons even under strongly positive (+1  $V_{RHE}$ ) potentials. As we later discuss,  
156 the ability to accumulate charge at positive potentials is critical to the efficient operation of  
157 the complete water splitting Z-scheme in photocatalyst sheets.  
158  
159

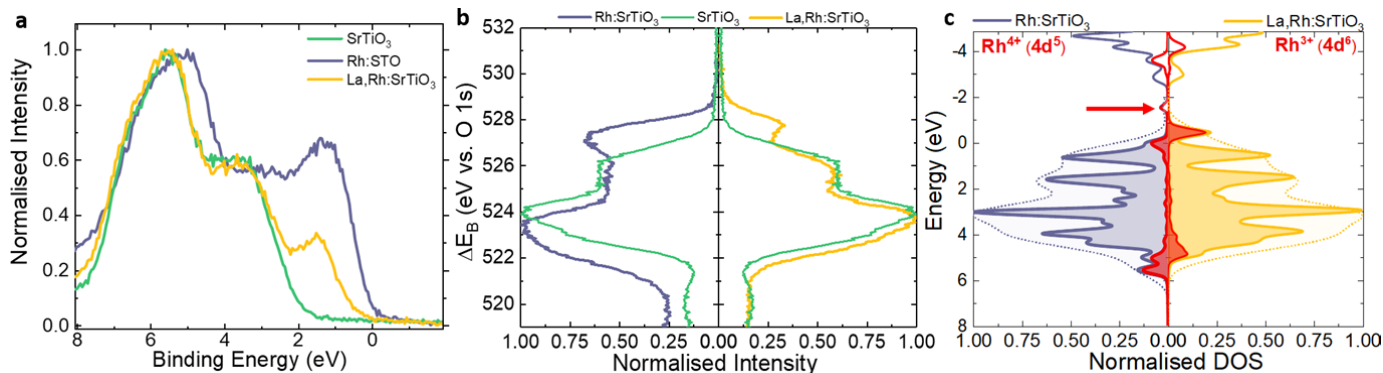


**Figure 3. Effect of Rh and La doping on theoretical and experimental band structure of SrTiO<sub>3</sub>.** (a) Valence XPS spectra of SrTiO<sub>3</sub>, Rh:SrTiO<sub>3</sub>, and La,Rh:SrTiO<sub>3</sub>. The larger area of the peak introduced by Rh doping in Rh:SrTiO<sub>3</sub> is attributed to increased surface segregation of Rh in Rh:SrTiO<sub>3</sub> (Supplementary Fig. S2.1, Table S1). (b) VB spectra of the samples on the  $\Delta E_B$  scale enable direct comparison of the energy of the Rh dopant states. (c) The density of states calculated by hybrid DFT, aligned using O 2p states and weighted by the elemental single electron ionisation cross-section for the Al K $\alpha$  X-rays used in our XPS studies. Rh 4d states are shown in red. To approximate further broadening, an additional gaussian broadening was applied to the peaks, leading to the envelope shown by the dotted line. Unlike XPS, DFT also gives the density of unoccupied states. The red arrow points to an unoccupied Rh state in the mid gap of Rh:SrTiO<sub>3</sub> that is absent in La,Rh:SrTiO<sub>3</sub>.

160 To better understand the link between the fundamental photophysical properties of  
 161 (La),Rh:SrTiO<sub>3</sub> and the oxidation state of Rh, we turn to DFT-supported VB XPS.  
 162 Comparing VB spectra of SrTiO<sub>3</sub>, Rh:SrTiO<sub>3</sub> and La,Rh:SrTiO<sub>3</sub> (Fig. 3a), we observe a  
 163 significant Fermi level ( $E_F$ ) shift in both Rh-doped oxides towards the effective VB edge,  
 164 consistent with p-type conductivity as observed by Kudo et al.<sup>34</sup>  $E_F$  of SrTiO<sub>3</sub>, Rh:SrTiO<sub>3</sub> and  
 165 La,Rh:SrTiO<sub>3</sub> is located  $\sim$ 1.8 eV,  $\sim$ 0.1 eV and  $\sim$ 0.3 eV above their respective VB edges  
 166 (linear extrapolation see Supplementary Fig. S2.1f). As a result, all peaks shift in accordance  
 167 with the observed Fermi level change seen in the VB spectrum (Supplementary Figure  
 168 S2.2a), consistent with previous observations of Rh doped oxides.<sup>35,36</sup> This effect prevents  
 169 direct comparison of relative energies of Rh states in the VB region on the binding energy  
 170 ( $E_B$ ) scale.<sup>35</sup> However, the binding energy relative to lattice O<sup>2-</sup> in the O 1s spectrum ( $\Delta E_B$  vs  
 171 O 1s) should be independent of this effect<sup>36</sup> (Supplementary Figure S2.2a and accompanying  
 172 equation). Comparison of the VB spectra of doped and undoped materials, plotted relative to  
 173 the lattice O<sup>2-</sup> binding energy (Fig. 3b), allows us to see that Rh doping introduces states  
 174 above the VB maximum and below the VB minimum of SrTiO<sub>3</sub>, leading to a broadening of  
 175 the VB envelope and a narrowing of the effective band gap, consistent with our observations  
 176 in Fig. 1a. Closer inspection of the region around the VB maximum (Supplementary Fig.  
 177 S2.2b) shows that the states introduced by Rh doping are shifted to higher energy upon La  
 178 co-doping. The same effect is also observed when Rh:SrTiO<sub>3</sub> is reduced in a hydrogen  
 179 atmosphere (Supplementary Figure S2.3f), implying that this shift is the result of Rh<sup>4+</sup>  
 180 reduction rather than any additional orbital contribution from La. This effect is consistent  
 181 with the red shift in the effective band edge observed when Rh:SrTiO<sub>3</sub> is reduced (Fig. 2a,b).



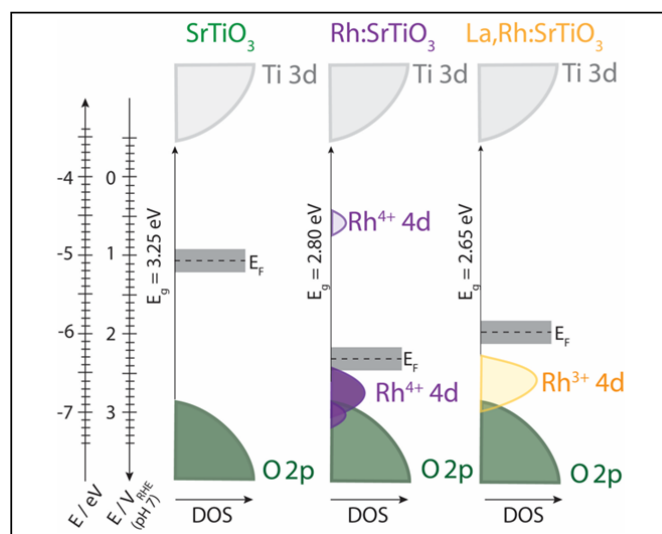


**Figure 4. A simplified electronic structure model.** Energy band diagrams of SrTiO<sub>3</sub>, Rh:SrTiO<sub>3</sub> and La,Rh:SrTiO<sub>3</sub> determined from the combined results of our XPS, UV-vis, (spectro)electrochemistry measurements and DFT calculations. Plotted is the density of states (DOS) on the absolute energy scale as well as on the reversible hydrogen electrode (RHE) scale at pH 7. Fermi level positions ( $E_F$ ) and band gap energies ( $E_g$ ) and the position of the vacant Rh<sup>4+</sup> mid gap level in Rh:SrTiO<sub>3</sub> are also indicated. See main text for more details.

182 To verify our analysis of the VB spectra, and to provide insight into the nature of the Rh  
 183 states introduced by doping, we turned to hybrid DFT. The HSE06 functional was combined  
 184 with an unprecedentedly large 3x3x3 supercell to enable accurate reproduction of the nominal  
 185 Rh-doping concentration to calculate and compare the electronic structure of doped, co-doped  
 186 and undoped SrTiO<sub>3</sub> (see Methods for further details). The calculated densities of states  
 187 (DOS) for the VB region of Rh:SrTiO<sub>3</sub> and La,Rh:SrTiO<sub>3</sub> (Fig. 3c) reveal that the broadening  
 188 of the VB region observed experimentally upon Rh doping is caused by the introduction of  
 189 Rh 4d states above the VB maximum and below the VB minimum of SrTiO<sub>3</sub>. Moreover, DFT  
 190 accurately predicts that in Rh:SrTiO<sub>3</sub>, Rh 4d states are more deeply situated than in  
 191 La,Rh:SrTiO<sub>3</sub>, which is verified by our experiments as detailed above (Fig. 1a and 3b). No La  
 192 orbital character is observed near the band edges (Supplementary Fig. S6.1b), consistent with  
 193 the concept that La<sup>3+</sup> induces the reduction of Rh<sup>4+</sup> via an ionic charge compensation  
 194 mechanism but does not directly alter band edge composition.<sup>29</sup> Most strikingly, a vacant mid  
 195 gap state with Rh 4d character is observed in Rh:SrTiO<sub>3</sub> (red arrow, Fig. 3c) which is absent  
 196 in La,Rh:SrTiO<sub>3</sub>. As this state does not have La orbital character, and an analogous effect can  
 197 be achieved by introducing an electron to Rh:SrTiO<sub>3</sub> in the presence of a compensating  
 198 background charge (which localises on Rh<sup>4+</sup> during optimisation, Supplementary Fig. S6.1d,  
 199 S6.2), we attribute this change to Rh<sup>4+</sup> reduction. Further, integration of the Rh 4d DOS  
 200 shows that the density of filled Rh 4d states at the VB edge effectively increases by one  
 201 electron upon reduction. This indicates that the Rh 4d electronic structure re-arranges as an  
 202 electron is added to Rh<sup>4+</sup> and the mid gap state is incorporated into the VB (for discussion see  
 203 Supplementary Fig. S6.2, S6.3).

204 Figure 4 summarises energy band diagrams of SrTiO<sub>3</sub> and its doped equivalents determined  
 205 from our SEC and DFT-supported XPS experiments. From DFT we obtain electron affinities,<sup>37</sup>  
 206 which are in good agreement with literature values for CB edge energies ( $E_{CB}$ ) of SrTiO<sub>3</sub>,<sup>37</sup>  
 207 and indicate that  $E_{CB}$  is largely insensitive to doping (Supplementary Fig. S6.4). As DFT  
 208 calculations often slightly underestimate  $E_g$ , we use our UV-vis spectra (Fig. 1a) to position  
 209 the VB edge energies on an absolute energy scale, in reasonable agreement with our  
 210 calculated ionisation potentials (Supplementary Fig. S6.4). From VB XPS (Fig. 3a), we

211 estimate the Fermi level position relative to the VB (in the absence of band bending) and find  
212 it to be in excellent agreement with independent measurements of a very positive flatband  
213 potential of La,Rh:SrTiO<sub>3</sub> photocatalyst sheets (+1.8  $V_{RHE}$ ) using impedance spectroscopy,  
214 consistent with reported p-type character.<sup>24,30,31</sup> Finally, we estimate the reduction potential of  
215 Rh<sup>4+</sup> states using the half-wave potential obtained from SEC (Supplementary Fig. S4b) and  
216 combine it with our DFT results to locate the vacant mid-gap state.

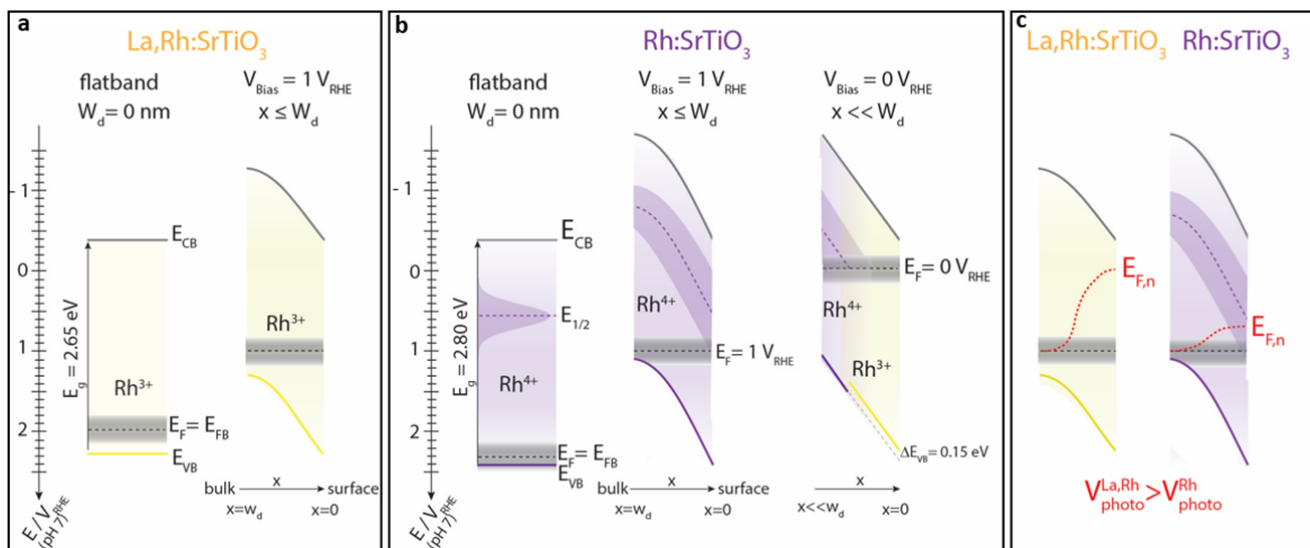


**Figure 5. A simple surface depletion model explaining the in-situ charge carrier dynamics of (La,Rh):SrTiO<sub>3</sub> photocatalyst sheets.** Model of surface depletion in La,Rh:SrTiO<sub>3</sub> (a) and Rh:SrTiO<sub>3</sub> (b) at different applied potentials in the dark. The flatband condition ( $E_F = E_{FB}$ ) for both materials is adapted from Fig. 4. At  $1 V_{RHE}$ , there is significant band bending in both La,Rh:SrTiO<sub>3</sub> and Rh:SrTiO<sub>3</sub> (with  $W_d$  indicating the space charge layer width). However, in Rh:SrTiO<sub>3</sub>, the Fermi level ( $E_F$ ) does not exceed the reduction potential of the vacant  $Rh^{4+}$  level ( $E_{1/2}$ , purple dashed line), leading to Rh adopting the 4+ oxidation state in the entire material and in the depletion layer ( $x < W_d$ ). At  $0 V_{RHE}$ , the energy of  $Rh^{4+}$  at the surface of the depletion region ( $d \ll W_d$ ) falls below the Fermi level and  $Rh^{4+}$  becomes reduced, leading to a re-organisation of the Rh 4d states – adopting the electronic configuration of a reduced Rh:SrTiO<sub>3</sub> (indicated by yellow colouring), which is almost identical to that of La,Rh:SrTiO<sub>3</sub>. This is corroborated by a 0.15 eV red-shift in the effective band gap that we observe in our SEC experiments (Fig. 2a). (c) Photovoltage build-up in La,Rh:SrTiO<sub>3</sub> and Rh:SrTiO<sub>3</sub> under illumination at positive device operation potentials. Here, conduction band electrons can accumulate in La,Rh:SrTiO<sub>3</sub> due to strong downward band bending leading to effective charge separation. This is indicated by a quasi-Fermi level for electrons ( $E_{F,n}$ ) reaching towards the CB. In Rh:SrTiO<sub>3</sub>, a similarly strong potential drop develops at the surface, however, trapping processes likely related to the trapping of electrons by  $Rh^{4+}$  states prevent the accumulation of electrons, indicated by a quasi-Fermi level pinned to the  $Rh^{4+}$  redox potential. This in turn leads to smaller photovoltage developing in Rh:SrTiO<sub>3</sub>.

217 In Figure 5, we use the energy band diagrams in Figure 4 to illustrate the expected potential-  
 218 dependence of depletion layer formation in (La,Rh):SrTiO<sub>3</sub>, and relate these to our potential-  
 219 dependent SEC, PIA and TA measurements (Fig. 2). A striking result of this analysis is that  
 220 in both La,Rh:SrTiO<sub>3</sub> (Fig. 5a) and Rh:SrTiO<sub>3</sub> (Fig. 5b), a strong potential drop at the  
 221 semiconductor-electrolyte liquid junction is created even at the most positive potentials  
 222 studied (e.g.  $1 V_{RHE}$ ) due to their strongly positive flatband potentials (Fig 4). The field in the  
 223 depletion region at these potentials appears to be sufficient to efficiently separate charge in  
 224 La,Rh:SrTiO<sub>3</sub>, as inducing a further volt of band bending (i.e. at  $0 V_{RHE}$ ) yields only a modest  
 225 increase in the photogeneration of long-lived CB electrons under operational conditions (Fig.  
 226 2e). This implies that the downward shift in flatland potentials induced by Rh doping drives  
 227 effective charge separation even at positive applied potentials. This is consistent with the  
 228 remarkably early onset potentials (up to  $1.2 V_{RHE}$ ) previously observed in photocatalyst sheet  
 229 half-electrodes.<sup>25</sup> However, despite a similar flatband potential to La,Rh:SrTiO<sub>3</sub>, Rh:SrTiO<sub>3</sub>  
 230 is unable to photogenerate long-lived electrons at equivalent positive potentials (i.e.  $1 V_{RHE}$ ).  
 231 Instead, Rh:SrTiO<sub>3</sub> shows a yield of CB electrons which tracks the redox wave originating  
 232 from  $Rh^{4+}$  reduction (Fig. 2f, Supplementary Fig. S4b), with the largest changes occurring  
 233 around  $E_{1/2}$  of the  $Rh^{4+}/Rh^{3+}$  redox couple. Only at potentials negative of this redox potential  
 234 do the yields and lifetimes of CB electrons in Rh:SrTiO<sub>3</sub> and La,Rh:SrTiO<sub>3</sub> converge. In  
 235 Figure 5c we use our model to explain this behaviour. At potentials positive of  $E_{1/2}$ , minority  
 236 carriers in Rh:SrTiO<sub>3</sub> are trapped and recombine via mid-gap  $Rh^{4+}$  states. The quasi-Fermi  
 237 level of electrons ( $E_{F,n}$ ) is therefore likely to be pinned to these mid-gap states, leading to a  
 238 diminished photovoltage in comparison to La,Rh:SrTiO<sub>3</sub> (Supplementary Fig. 7). At



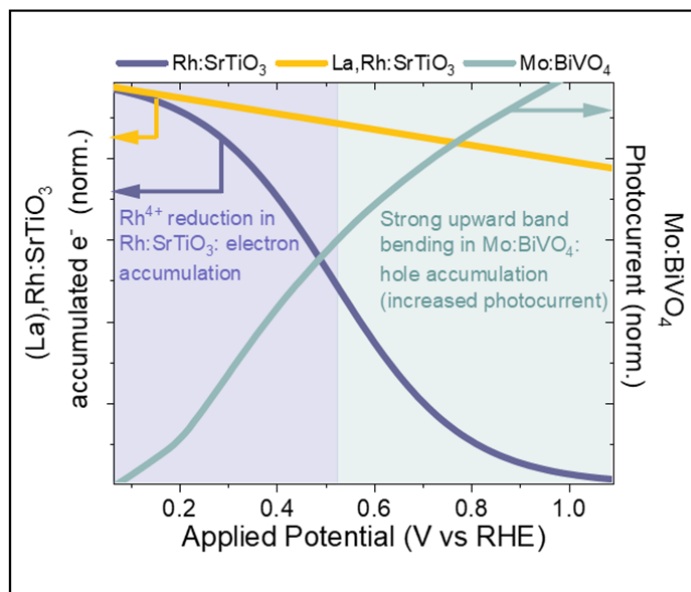


**Figure 6. The role of Rh oxidation state and La co-doping in determining the performance of a Mo:BiVO<sub>4</sub>/(La),Rh:SrTiO<sub>3</sub> Z-scheme device.** Electron accumulation under operational conditions in (La),Rh:SrTiO<sub>3</sub> (Fig. 2f) plotted alongside a normalised J-V curve for typical Mo:BiVO<sub>4</sub> photocatalyst sheets in the presence of a Fe/Ni based co-catalyst.<sup>17</sup>

239 potentials negative of  $E_{1/2}$ , Rh<sup>4+</sup> states in the depletion layer are reduced, and persistent CB  
 240 electrons are observed (Fig. 2d). Hence, La co-doping can be understood as obviating the  
 241 need for the strong negative potentials ( $\ll 0.52 V_{RHE}$ ) or chemically reducing  
 242 conditions<sup>23,25,27,38</sup> that would be otherwise required to reduce surface Rh<sup>4+</sup> states. This  
 243 suppresses electron trapping, leading to the build-up of a higher photovoltage due to the  
 244 accumulation of minority carriers on timescales of the water splitting reaction.  
 245 Due to current matching requirements, the operation of complete photocatalyst sheet devices  
 246 is thus also Rh oxidation state dependent. Hence, in a Rh:SrTiO<sub>3</sub>/Mo:BiVO<sub>4</sub> device, large  
 247 yields of persistent electrons in Rh:SrTiO<sub>3</sub> can solely be obtained closer to the flatband  
 248 potential of Mo:BiVO<sub>4</sub> (ca.  $0.1 V_{RHE}$ <sup>39</sup>) or, in other words, close to the onset of photocurrent  
 249 for an optimal Mo:BiVO<sub>4</sub> photoanode.<sup>40,41</sup> In contrast, in a La,Rh:SrTiO<sub>3</sub>/Mo:BiVO<sub>4</sub> device,  
 250 La fixes the Rh oxidation state to Rh<sup>3+</sup> and removes the Rh<sup>4+</sup> mid-gap level *without*  
 251 *compromising the position of the Fermi level*. This leads to accumulation of CB electrons  
 252 even at remarkably positive potentials. This is illustrated in Figure 6 where the population of  
 253 accumulated CB electrons in (La),Rh:SrTiO<sub>3</sub> sheets (taken from Fig. 2f) is plotted alongside  
 254 a JV curve of a previously reported typical Mo:BiVO<sub>4</sub> photocatalyst sheet half electrode.<sup>17</sup>  
 255 Figure 6 predicts that the crossing point of Rh:SrTiO<sub>3</sub>/Mo:BiVO<sub>4</sub> device would be at more  
 256 negative potentials, where the Rh:SrTiO<sub>3</sub> surface is only partially reduced and the predicted  
 257 photocurrent low. On the other hand, a La,Rh:SrTiO<sub>3</sub>/Mo:BiVO<sub>4</sub> crosses at a significantly  
 258 more positive potential, at which photogeneration of long-lived charge carriers is high in both  
 259 Mo:BiVO<sub>4</sub> and La,Rh:SrTiO<sub>3</sub>, enabling both efficient proton reduction and water oxidation.  
 260 The more positive crossing point of the respective half-cell J-E curves in turn leads to a Z-  
 261 scheme photocatalyst sheet device requiring a metal contact with a high work function (i.e.  
 262 Au), consistent with calculations in the work of Wang *et al.*<sup>26</sup> The carrier dynamics of this  
 263 interface are of significant interest. However, the surface selective nature of the  
 264 measurements presented here preclude study of the back contact.  
 265 It is remarkable that chemical reduction of Rh:SrTiO<sub>3</sub> does not compromise the position of  
 266 the Fermi level as would be expected from simply considering the filling of the Rh<sup>4+</sup> mid gap  
 267 level upon reduction in the absence of any reorganization. We therefore consider the

268 oxidation state dependent Rh 4d electronic structure to be a crucial and distinguishing  
269 operational parameter in this material, as conservation of the position of the Fermi level upon  
270 chemical reduction leads to extremely positive flatband potentials being observed in the Rh-  
271 doped and La,Rh co-doped materials alike. This drives strong band bending at the  
272 semiconductor/electrolyte interface in-situ, meaning that charge separation is limited by  
273 density of the vacant mid gap levels associated only with Rh<sup>4+</sup> rather than the strength or  
274 width of the depletion layer. Thus, co-doping with La reduces Rh<sup>4+</sup>; removing mid gap levels  
275 without strongly influencing band bending. This drives a positive shift in the crossing point  
276 of the complete Z-scheme device towards a crossing point where both water oxidation and  
277 proton reduction occurs efficiently.

278 In conclusion, by linking charge accumulation to electronic structure in (La),Rh:SrTiO<sub>3</sub> we  
279 are able to explain the record device operation of the La,Rh:SrTiO<sub>3</sub>/Mo:BiVO<sub>4</sub> photocatalyst  
280 sheets. We find that Rh doping narrows the effective optical gap of SrTiO<sub>3</sub> and induces a  
281 strong downward shift in flatband potential, successfully creating a p-type visible light  
282 absorber. Using Rh alone to dope the wide band gap absorber produces a vacant mid-gap Rh  
283 4d state. During illumination, this state prevents the accumulation of electrons near the  
284 conduction band and instead promotes charge trapping and recombination. Reduction of Rh<sup>4+</sup>  
285 leads to a reorganization of Rh 4d orbitals, integrating this state into the valence band region.  
286 While the reduction to Rh<sup>3+</sup> can be driven by negative applied potential or by a reductive  
287 annealing treatment, co-doping with La appears to be an elegant strategy to effectively and  
288 persistently mitigate the formation of the mid-gap state without compromising p-type  
289 character. In the absence of a mid-gap state, the strongly positive flatband potential of  
290 La,Rh:SrTiO<sub>3</sub> enables strong downward band bending even under relatively positive  
291 potentials (e.g. +1 V<sub>RHE</sub>), enabling bipolar charge accumulation in the device at potentials  
292 where both the n- and p-type semiconductors separate charge efficiently.

293 More broadly, this work identifies both electronic structure reorganisation and Fermi level  
294 effects as key parameters that must be considered in engineering novel functional visible light  
295 absorbing materials for photocatalysis. The insights gained herein lead to a deeper  
296 understanding of the interplay between electronic structure, dopant oxidation states, minority  
297 carrier lifetimes and device operation in cutting edge photocatalyst devices. Having identified  
298 the crucial role of co-doping in the function of the complete Z-scheme device, we note that a  
299 necessary prerequisite to succeeding in creating new band gap engineered visible light  
300 absorbers may be the choice of a perovskite (ABX<sub>3</sub>) host lattice, such as SrTiO<sub>3</sub>, where two  
301 cation sites can be substituted independently of one another in a crystal lattice that is  
302 structurally tolerant to doping. This represents a crucial break from studies on TiO<sub>2</sub>, where  
303 only one cation site can be substituted in a lattice that is itself less tolerant to doping.<sup>36</sup>

304

### 305 **Acknowledgements**

306 B.M thanks the EPSRC for a doctoral training partnership and the UK Solar Fuels Network  
307 for an exchange scholarship to the group of K.D. BM also thanks Prof. Rob Palgrave for  
308 discussion of his previous work on Rh doped TiO<sub>2</sub> and doped oxides and D.H.K Murthy for  
309 advice on sample choice and handling. S.S thanks the EPSRC for a doctoral training  
310 partnership. L.S. and J. R. D. acknowledge funding from the European Research Council  
311 (H2020-MSCA-IF-2016, Grant No. 749231 and AdG Intersolar, Grant No. 291482,  
312 respectively). Funding was also obtained from the Artificial Photosynthesis Project of the  
313 New Energy and Industrial Technology Development Organization. AR acknowledges the  
314 support from the Analytical Chemistry Trust Fund for her CAMS-UK Fellowship and from  
315 Imperial College London for her Imperial College Research Fellowship. K.D thanks the  
316 Artificial Photosynthesis Project of the New Energy and Industrial Technology Development  
317 Organization (NEDO) for support. R. G. thanks the Natural Sciences and Engineering

318 Research Council of Canada (NSERC) for operational funding (Grant No. RGPIN-2019-  
319 05521). A. K. thanks Imperial College for a Junior Research Fellowship, the EPSRC for a  
320 Capital Award Emphasising Support for Early Career Researchers and the Royal Society for  
321 an Equipment Grant (RSG\R1\180434)

322 **Author Contributions**

323 B.M. carried out all optical, SEM and XPS measurements and wrote the manuscript with help  
324 from L.S. and S.S. XPS measurements and interpretation of results were supervised by A.R.  
325 and D.J.P. Q.W. synthesised all materials, fabricated all devices and performed XRD. K.T.B.  
326 performed all calculations of doped, co-doped and undoped STO, with the exception of the  
327 DFT study of Rh doping concentration, which was performed by R.G.C. L.S supervised this  
328 work, guided SEM, EDX and spectroelectrochemical measurements, oversaw data  
329 interpretation and manuscript preparation, and conceptualised Figures 4, 5 and 6. R.G. and  
330 A.K. trained B.M. and supervised optical measurements. T.H. co-supervised this work and  
331 K.D. and J.R.D. directed the research. All authors commented on the manuscript.

332 **Corresponding author**

333 Correspondence to Dr Ludmilla Steier. l.steier@imperial.ac.uk

334 **Competing interests**

335 The authors declare no competing interests.

336 **Data Availability**

337 The data presented in the main body of this paper is available in csv format on Zenodo at  
338 <http://doi.org/10.5281/zenodo.4063942> and source data is available in opj format also on  
339 Zenodo at <http://doi.org/10.5281/zenodo.4071556>. Both can be used under the Creative  
340 Commons Attribution licence 4.0.

341

342

## 343 **Methods**

344

345 **Synthesis of Rh and La,Rh:SrTiO<sub>3</sub>:** Rh:SrTiO<sub>3</sub> and La,Rh:SrTiO<sub>3</sub> were synthesised by a previously  
346 reported two step solid state reaction.<sup>25,42</sup> In the first step, rutile TiO<sub>2</sub> (Kanto Chemicals, 99.0%) and  
347 SrCO<sub>3</sub> (Kanto Chemicals, 99.9%, calcined in air at 573 K for 1 h) were ground in a mortar to obtain a  
348 mixture with a Sr/Ti ratio of 1.05. The mixture was then calcined at 1423 K for 10 h to produce  
349 SrTiO<sub>3</sub>. In the second step, SrTiO<sub>3</sub> was ground in ethanol with Rh<sub>2</sub>O<sub>3</sub> (Kanto Chemicals, 99.9%) and  
350 calcined at 1373 K for 6 h to make Rh:SrTiO<sub>3</sub>. For La,Rh:SrTiO<sub>3</sub> fabrication, both La<sub>2</sub>O<sub>3</sub> (Kanto  
351 Chemicals, 99.99%, freshly calcined in air at 1273 K for 12 h) and Rh<sub>2</sub>O<sub>3</sub> (Kanto Chemicals, 99.9%)  
352 were calcined at 1373 K for 6 h. In both cases, La and Rh was added such that the nominal doping  
353 concentration (i.e [Rh]/([Rh]+[Ti]) or [La]/([La]+[Sr]) was 4 mol%. H<sub>2</sub>-Rh:SrTiO<sub>3</sub> was produced by  
354 annealing Rh:SrTiO<sub>3</sub> powder at 573 K in a hydrogen atmosphere for two hours. For transient  
355 absorption scavenger studies, films were fabricated directly from powders by dispersing 50 mg of  
356 powder in water, drop casting on to glass and calcining at 673 K for 1 h.

357 **Fabrication of photocatalyst sheets:** (La),Rh:SrTiO<sub>3</sub> photocatalyst sheets were fabricated by a  
358 modified particle transfer method. The procedure was identical to previous reports except that  
359 Mo:BiVO<sub>4</sub> particles were omitted and a much thicker Au layer (ca. 2 μm as opposed to ca. 350 nm)  
360 was used to create a continuously conductive back contact. Doped SrTiO<sub>3</sub> (20 mg) was suspended in  
361 isopropanol (99.9%, 0.5 ml), drop-cast on a glass substrate (3×3 cm<sup>2</sup>) and left to dry at room  
362 temperature overnight. The Au back contact was then deposited by thermal vacuum evaporation  
363 (VFR-200M/ERH, ULVAC KIKO) at an evaporation rate of approximately 20 nm s<sup>-1</sup> at a base  
364 pressure of 2.6×10<sup>-3</sup> Pa. The exposed Au surface was then bonded to a second glass plate (3×3 cm<sup>2</sup>)  
365 with double sided carbon tape and lifted off the primary glass plate. The resulting photocatalyst sheet  
366 was then ultrasonicated twice in distilled water for 2 minutes to remove any unattached particles.

367 **Scanning electron microscopy (SEM):** SEM images were taken on a LEO GEMINI 1525  
368 microscope using a 1.5 keV electron beam and a secondary electron detector. As the back Au contact  
369 in the photocatalyst sheets provides a highly conductive pathway for charge, no conductive coating  
370 was required. EDX was performed on the same instrument using an Oxford Instruments X-act  
371 detector at a beam voltage of 20 keV and a 60 mm aperture.

372 **X-ray photoelectron spectroscopy (XPS):** XPS was performed on a Thermo Scientific K-alpha+  
373 instrument. Powdered samples were attached to a stainless-steel plate using conductive carbon tape.  
374 The instrument uses monochromated and microfocused Al Kα (hν = 1486.6 eV) radiation to eject  
375 photoelectrons which are then analysed using a 180° double-focusing hemispherical analyser with a  
376 2D detector. Spectra were collected at 2×10<sup>-9</sup> mbar base pressure. A flood gun was used to minimize  
377 sample charging. All samples were referenced against the C-C peak of adventitious carbon in the C 1s  
378 spectrum at a binding energy of 284.8 eV to correct for any charge that is not neutralised by the flood  
379 gun. Further effects were then accounted for by taking the separation from the O 1s oxide peak. Data  
380 was analysed using the CASA XPS package.

381 **Ultraviolet-visible absorption spectroscopy and spectroelectrochemistry:** Reflectance spectra of  
382 the photocatalyst sheets were collected using a Shimadzu UV-vis 2600 spectrophotometer equipped  
383 with an integrating sphere, using a disk of pressed barium sulphate as a 100% reflecting reference.  
384 The resulting diffuse reflectance spectra were then converted to a unit proportional to absorbance  
385 using the Kubelka-Munk function,  $F(R) = \frac{k}{s} = \frac{(1-R)^2}{2R}$ . Where  $k$  and  $s$  respectively correspond to  
386 absorption and scattering coefficients and  $R$  corresponds to the reflectance (the fraction of light  
387 reflected in comparison to the fully scattering BaSO<sub>4</sub> reference). For spectroelectrochemical  
388 measurements, photocatalyst sheets were measured in a quartz cuvette in three-electrode  
389 configuration using an Ag/AgCl (sat'd KCl) reference electrode, a platinum mesh counter electrode  
390 and the doped SrTiO<sub>3</sub> working electrodes in 0.1 M Na<sub>2</sub>SO<sub>4</sub> electrolyte (pH 7). Potentials were applied  
391 using a Metrohm Autolab PGSTAT 101 potentiostat. Reflection and refraction from the cuvette do  
392 not change with applied potential and so did not contribute to the observed change in the Kubelka-

393 Munk function. A small offset at 820 nm is visible due to a change in detector and a low background  
394 level of reflected light in this experiment.

395 **Hybrid Density functional calculations:** All calculations are performed using the VASP package.<sup>43</sup>  
396 For doping calculations a 3x3x3 supercell was created. In the case of co-doping all symmetry  
397 inequivalent positions of the dopants were explored, although no qualitative and very little  
398 quantitative differences were found. We therefore use a single configuration for presenting our results.  
399 For relaxation of atomic positions the PBEsol functional<sup>44</sup>, projector augmented pseudopotentials<sup>45</sup>,  
400 and a cut-off energy of 500 eV, with k-point sampling defined as an evenly spaced grid in reciprocal  
401 space with a density scaled to the unit cell size were used to achieve uniform sampling with a target  
402 length cut-off of 10 Å, as described by Moreno and Soler<sup>46</sup>. The relaxed structures were then used for  
403 input to hybrid DFT calculations using the HSE06 functional<sup>44</sup> to calculate accurate electronic  
404 structure.

405 **Diffuse reflectance transient absorption and photoinduced absorption:** Transient absorption and  
406 photoinduced absorption measurements were carried out on a home built setup described in our  
407 previous publications.<sup>47</sup> Briefly, micro-second to second transient absorption decays were acquired by  
408 measuring the diffuse reflectance of the opaque samples studied herein. A Nd:YAG laser (OPOTEK  
409 Opolette 355 II, 7 ns pulse width) was used as the excitation source, producing 355 nm light that was  
410 transmitted to the sample using a liquid light guide. An excitation power density of 400 μJ/cm<sup>2</sup> was  
411 typically used in conjunction with a laser repetition rate of 0.8 Hz. Probe light was generated by a  
412 100 W Bentham IL1 quartz halogen lamp. Long pass filters (Comar Instruments) and an IR filter  
413 (H<sub>2</sub>O, 5 cm path length) were positioned between the lamp and sample to minimise short wavelength  
414 irradiation and heating of the sample. Diffuse reflectance from the sample was collected and relayed  
415 to a monochromator (Oriel Cornerstone 130) through a long pass filter to select the probe wavelength.  
416 Acquisitions were triggered by a photodiode (Thorlabs DET10A) exposed to laser scatter. A Si  
417 photodiode (Hamamatsu S3071) was used as a detector in the visible region and an InGaAs diode  
418 (Hamamatsu G10899-03K) in the near IR. Data at times faster than 2 ms were amplified by custom  
419 electronics and recorded by an oscilloscope (Tektronics DPO3012) while data slower than 2 ms was  
420 simultaneously recorded on a National Instrument DAQ card (NI USB-6251). Kinetic traces were  
421 typically obtained from the average of 100 laser pulses. Data was acquired and processed using  
422 software written in the LabVIEW environment (Austin Consultants). Photoinduced absorption data,  
423 were collected with the same setup replacing the laser pulse by a continuous wave illumination of a  
424 365 nm LED at an intensity of 8 mW cm<sup>-2</sup>, corresponding to ½ sun of absorbed photons assuming a  
425 sharp absorption edge at 470 nm. The percentage change in reflectance was calculated according to  
426 pioneering work by Wilkinson and co-workers.<sup>48</sup> Here the fractional change in reflected light due to  
427 transient absorption is:

428

$$R_t = \frac{V_t - V_0}{V_0}$$

429 Where  $V_0$  is the voltage arising on Si photodiode from the probe beam before the pump,  $V_t$  is the  
430 voltage on the diode at time  $t$  after the pump. The % change in absorption (% Abs.) is thus:

431

$$\% Abs = (1 - R_t) \cdot 100$$

432

433 The changes of reflectance observed were low, with the largest signals being on the order of 1%. This  
434 enabled the transient signal to be taken as directly proportional to the concentration of excited state  
435 species.<sup>49</sup>

436

437

438 **References**

- 439 1. Fujishima, A., Zhang, X. & Tryk, D. A. TiO<sub>2</sub> photocatalysis and related surface  
440 phenomena. *Surface Science Reports* vol. 63 515–582 (2008).
- 441 2. Pai, Y. Y., Tylan-Tyler, A., Irvin, P. & Levy, J. Physics of SrTiO<sub>3</sub> - based  
442 heterostructures and nanostructures: A review. *Reports on Progress in Physics* vol. 81  
443 (2018).
- 444 3. Goto, Y. *et al.* A Particulate Photocatalyst Water-Splitting Panel for Large-Scale Solar  
445 Hydrogen Generation. *Joule* **2**, 509–520 (2018).
- 446 4. Zhao, Z. *et al.* Electronic structure basis for enhanced overall water splitting  
447 photocatalysis with aluminum doped SrTiO<sub>3</sub> in natural sunlight. *Energy Environ. Sci.*  
448 **12**, 1385–1395 (2019).
- 449 5. Abe, R. Recent progress on photocatalytic and photoelectrochemical water splitting  
450 under visible light irradiation. *J. Photochem. Photobiol. C Photochem. Rev.* **11**, 179–  
451 209 (2011).
- 452 6. Khan, S. U. M., Al-Shahry, M. & Ingler, W. B. Efficient photochemical water splitting  
453 by a chemically modified n-TiO<sub>2</sub>. *Science (80-. )*. **297**, 2243–2245 (2002).
- 454 7. Asahi, R., Morikawa, T., Ohwaki, T., Aoki, K. & Taga, Y. Visible-light photocatalysis  
455 in nitrogen-doped titanium oxides. *Science (80-. )*. **293**, 269–271 (2001).
- 456 8. Konta, R., Ishii, T., Kato, H. & Kudo, A. Photocatalytic activities of noble metal ion  
457 doped SrTiO<sub>3</sub> under visible light irradiation. *J. Phys. Chem. B* **108**, 8992–8995 (2004).
- 458 9. Herrmann, J. M., Disdier, J. & Pichat, P. Effect of chromium doping on the electrical  
459 and catalytic properties of powder titania under UV and visible illumination. *Chem.*  
460 *Phys. Lett.* **108**, 618–622 (1984).
- 461 10. Dagherir, R., Drogui, P. & Robert, D. Modified TiO<sub>2</sub> for environmental photocatalytic  
462 applications: A review. *Ind. Eng. Chem. Res.* **52**, 3581–3599 (2013).
- 463 11. Sakatani, Y. *et al.* Metal ion and N co-doped TiO<sub>2</sub> as a visible-light photocatalyst. *J.*  
464 *Mater. Res.* **19**, 2100–2108 (2004).
- 465 12. Kudo, A., Niishiro, R., Iwase, A. & Kato, H. Effects of doping of metal cations on  
466 morphology, activity, and visible light response of photocatalysts. *Chem. Phys.* **339**,  
467 104–110 (2007).
- 468 13. Torres, G. R., Lindgren, T., Lu, J., Granqvist, C. G. & Lindquist, S. E.  
469 Photoelectrochemical study of nitrogen-doped titanium dioxide for water oxidation. *J.*  
470 *Phys. Chem. B* **108**, 5995–6003 (2004).
- 471 14. Sivula, K. & Van De Krol, R. Semiconducting materials for photoelectrochemical  
472 energy conversion. *Nat. Rev. Mater.* **1**, 15010 (2016).
- 473 15. Tilley, S. D., Cornuz, M., Sivula, K. & Grätzel, M. Light-induced water splitting with  
474 hematite: Improved nanostructure and iridium oxide catalysis. *Angew. Chemie - Int.*  
475 *Ed.* **49**, 6405–6408 (2010).
- 476 16. Zhong, D. K. & Gamelin, D. R. Photo-electrochemical water oxidation by cobalt  
477 catalyst (‘Co-Pi’)/ $\alpha$ -Fe<sub>2</sub>O<sub>3</sub> composite photoanodes: Oxygen evolution and resolution of  
478 a kinetic bottleneck. *J. Am. Chem. Soc.* **132**, 4202–4207 (2010).
- 479 17. Kuang, Y. *et al.* Ultrastable low-bias water splitting photoanodes via photocorrosion  
480 inhibition and in situ catalyst regeneration. *Nat. Energy* **2**, 16191 (2017).
- 481 18. Kim, J. H. *et al.* Awakening Solar Water Splitting Activity of ZnFe<sub>2</sub>O<sub>4</sub> Nanorods by  
482 Hybrid Microwave Annealing. *Adv. Energy Mater.* **5**, 1401933 (2015).
- 483 19. Li, Y. *et al.* Cobalt phosphate-modified barium-doped tantalum nitride nanorod  
484 photoanode with 1.5% solar energy conversion efficiency. *Nat. Commun.* **4**, 2566  
485 (2013).
- 486 20. Minegishi, T., Nishimura, N., Kubota, J. & Domen, K. Photoelectrochemical  
487 properties of LaTiO<sub>2</sub>N electrodes prepared by particle transfer for sunlight-driven  
488 water splitting. *Chem. Sci.* **4**, 1120–1124 (2013).

- 489 21. Maeda, K. *et al.* Photocatalyst releasing hydrogen from water. *Nature* **440**, 295 (2006).
- 490 22. Luo, J. *et al.* Cu<sub>2</sub>O Nanowire Photocathodes for Efficient and Durable Solar Water  
491 Splitting. *Nano Lett.* **16**, 1848–1857 (2016).
- 492 23. Wang, Q., Hisatomi, T., Ma, S. S. K., Li, Y. & Domen, K. Core/shell structured La-  
493 and Rh-Codoped SrTiO<sub>3</sub> as a hydrogen evolution photocatalyst in Z-scheme overall  
494 water splitting under visible light irradiation. *Chem. Mater.* **26**, 4144–4150 (2014).
- 495 24. Wang, Q. *et al.* Z-scheme water splitting using particulate semiconductors  
496 immobilized onto metal layers for efficient electron relay. *J. Catal.* **328**, 308–315  
497 (2015).
- 498 25. Wang, Q. *et al.* Scalable water splitting on particulate photocatalyst sheets with a  
499 solar-to-hydrogen energy conversion efficiency exceeding 1%. *Nat. Mater.* **15**, 611–  
500 615 (2016).
- 501 26. Wang, Q. *et al.* Particulate photocatalyst sheets based on carbon conductor layer for  
502 efficient Z-scheme pure-water splitting at ambient pressure. *J. Am. Chem. Soc.* **139**,  
503 1675–1683 (2017).
- 504 27. Kawasaki, S. *et al.* Elucidation of Rh-induced In-gap states of Rh:SrTiO<sub>3</sub> visible-light-  
505 driven photocatalyst by soft X-ray spectroscopy and first-principles calculations. *J.*  
506 *Phys. Chem. C* **116**, 24445–24448 (2012).
- 507 28. Abe, Y., Kato, K., Kawamura, M. & Sasaki, K. Rhodium and Rhodium Oxide Thin  
508 Films Characterized by XPS. *Surf. Sci. Spectra* **8**, 117–125 (2001).
- 509 29. Modak, B. & Ghosh, S. K. Exploring the Role of La Codoping beyond Charge  
510 Compensation for Enhanced Hydrogen Evolution by Rh-SrTiO<sub>3</sub>. *J. Phys. Chem. B*  
511 **119**, 11089–11098 (2015).
- 512 30. Murthy, D. H. K. *et al.* Revealing the role of the Rh valence state, la doping level and  
513 Ru cocatalyst in determining the H<sub>2</sub> evolution efficiency in doped SrTiO<sub>3</sub>  
514 photocatalysts. *Sustain. Energy Fuels* **3**, 208–218 (2019).
- 515 31. Iwashina, K. & Kudo, A. Rh-doped SrTiO<sub>3</sub> photocatalyst electrode showing cathodic  
516 photocurrent for water splitting under visible-light irradiation. *J. Am. Chem. Soc.* **133**,  
517 13272–13275 (2011).
- 518 32. Godin, R., Kafizas, A. & Durrant, J. R. Electron transfer dynamics in fuel producing  
519 photosystems. *Current Opinion in Electrochemistry* vol. 2 136–143 (2017).
- 520 33. Murthy, D. H. K. *et al.* Revealing the role of the Rh valence state, la doping level and  
521 Ru cocatalyst in determining the H<sub>2</sub> evolution efficiency in doped SrTiO<sub>3</sub>  
522 photocatalysts. *Sustain. Energy Fuels* **3**, 208–218 (2019).
- 523 34. Iwashina, K. & Kudo, A. Rh-doped SrTiO<sub>3</sub> photocatalyst electrode showing cathodic  
524 photocurrent for water splitting under visible-light irradiation. *J. Am. Chem. Soc.* **133**,  
525 13272–13275 (2011).
- 526 35. Oropeza, F. E. & Egdell, R. G. Control of valence states in Rh-doped TiO<sub>2</sub> by Sb co-  
527 doping: A study by high resolution X-ray photoemission spectroscopy. *Chem. Phys.*  
528 *Lett.* **515**, 249–253 (2011).
- 529 36. Glover, E. N. K., Ellington, S. G., Sankar, G. & Palgrave, R. G. The nature and effects  
530 of rhodium and antimony dopants on the electronic structure of TiO<sub>2</sub>: Towards design  
531 of Z-scheme photocatalysts. *J. Mater. Chem. A* **4**, 6946–6954 (2016).
- 532 37. Fujisawa, J. ichi, Eda, T. & Hanaya, M. Comparative study of conduction-band and  
533 valence-band edges of TiO<sub>2</sub>, SrTiO<sub>3</sub>, and BaTiO<sub>2</sub> by ionization potential  
534 measurements. *Chem. Phys. Lett.* **685**, 23–26 (2017).
- 535 38. Kawasaki, S. *et al.* Epitaxial Rh-doped SrTiO<sub>3</sub> thin film photocathode for water  
536 splitting under visible light irradiation. *Appl. Phys. Lett.* **101**, 033910 (2012).
- 537 39. Rettie, A. J. E. *et al.* Combined charge carrier transport and photoelectrochemical  
538 characterization of BiVO<sub>4</sub> single crystals: Intrinsic behavior of a complex metal oxide.

- 539 *J. Am. Chem. Soc.* **135**, 11389–11396 (2013).
- 540 40. Ma, Y., Le Formal, F., Kafizas, A., Pendlebury, S. R. & Durrant, J. R. Efficient  
541 suppression of back electron/hole recombination in cobalt phosphate surface-modified  
542 undoped bismuth vanadate photoanodes. *J. Mater. Chem. A* **3**, 20649–20657 (2015).
- 543 41. Zachäus, C., Abdi, F. F., Peter, L. M. & Van De Krol, R. Photocurrent of BiVO<sub>4</sub> is  
544 limited by surface recombination, not surface catalysis. *Chem. Sci.* **8**, 3712–3719  
545 (2017).
- 546 42. Wang, Q. *et al.* Particulate photocatalyst sheets based on carbon conductor layer for  
547 efficient Z-scheme pure-water splitting at ambient pressure. *J. Am. Chem. Soc.* **139**,  
548 1675–1683 (2017).
- 549 43. Joubert, D. *From ultrasoft pseudopotentials to the projector augmented-wave method.*  
550 *Physical Review B - Condensed Matter and Materials Physics* vol. 59 (1999).
- 551 44. Perdew, J. P. *et al.* Generalized gradient approximation for solids and their surfaces.  
552 (2007) doi:10.1103/PhysRevLett.100.136406.
- 553 45. Kresse, G. & Furthmüller, J. Efficient iterative schemes for ab initio total-energy  
554 calculations using a plane-wave basis set. *Phys. Rev. B - Condens. Matter Mater. Phys.*  
555 **54**, 11169–11186 (1996).
- 556 46. Moreno, J. & Soler, J. M. Optimal meshes for integrals in real- and reciprocal-space  
557 unit cells. *Phys. Rev. B* **45**, 13891–13898 (1992).
- 558 47. Godin, R., Wang, Y., Zwijnenburg, M. A., Tang, J. & Durrant, J. R. Time-Resolved  
559 Spectroscopic Investigation of Charge Trapping in Carbon Nitrides Photocatalysts for  
560 Hydrogen Generation. *J. Am. Chem. Soc.* **139**, 5216–5224 (2017).
- 561 48. Wilkinson, F. Diffuse reflectance laser flash photolysis. *J. Photochem.* **17**, 52 (1981).
- 562 49. Kessler, R. W., Oelkrug, D. & Wilkinson, F. *The Detection of Transient Spectra within*  
563 *Polycrystalline Samples Using the New Technique of Diffuse Reflectance Flash*  
564 *Photolysis.*
- 565
- 566



